Journal of Materials Chemistry A

ROYAL SOCIETY OF CHEMISTRY

PAPER

View Article Online
View Journal | View Issue

Cite this: *J. Mater. Chem. A*, 2025, **13**, 2309

Atomic insight into Li^+ ion transport in amorphous electrolytes $Li_xAlO_yCl_{3+x-2y}$ ($0.5 \leq x \leq 1.5$, $0.25 \leq y \leq 0.75$)†

Qifan Yang,[ab] Jing Xu,[ac] Xiao Fu,[ab] Jingchen Lian,[ab] Liqi Wang,[ac] Xuhe Gong,[ad] Ruijuan Xiao *[abc] and Hong Li *[abc]

Received 3rd September 2024
Accepted 17th November 2024

DOI: 10.1039/d4ta06234e

rsc.li/materials-a

The recent study of viscoelastic amorphous oxychloride electrolytes has opened up a new field of research for solid-state electrolytes. In this work, we chose a Li–Al–O–Cl system containing disordered structures with varying O/Cl ratios and Li^+ contents to study their structural characteristics and ion transport mechanism using *ab initio* molecular dynamics (AIMD) simulation and machine learning interatomic potential based molecular dynamics (MLIP-based MD) simulation. It is found that O-doping results in the presence of a skeleton of Al-chains formed by AlOCl tetrahedra and an increase in glass forming ability, causing Cl atoms' rotation around centered-Al within the tetrahedron thus facilitating the motion of Li^+ ions. However, a further increase in the O/Cl ratio decreases the number of rotating Cl atoms, weakening the transport of Li^+. So increasing glass forming ability without reducing Cl content or by methods through controlling synthesis conditions, is useful to promote Li^+ ion conduction of oxychloride electrolytes.

1 Introduction

At present, the fast development of lithium-ion batteries (LIBs) with excellent properties[1] has promoted the progress of industries.[2,3] Compared to the commonly used LIBs, solid-state batteries (SSBs) with solid-state electrolytes (SSEs) have better safety and greater potential.[4–7] SSEs can be divided into polymer SSEs, inorganic SSEs and their composites.[8,9] Among them, inorganic SSEs consist of two structural types: crystalline and amorphous.[10,11] Up to now, crystalline SSEs have been well explored. Li argyrodites,[12–14] $Li_{10}GeP_2S_{12}$ (LGPS),[15,16] the NASICON structure of $LiM_2(PO_4)_3$ (M = Ge, Ti, Sn, Hf, Zr) compositions,[17] the garnet structure of $Li_xLa_3M_2O_{12}$ ($5 \leq x \leq 7$, M = Nb, Ta, Sb, Zr, Sn) compositions[18,19] and so on exhibit ionic conductivity similar to that of liquid electrolytes. Compared to crystalline SSEs, there is much less exploration of amorphous SSEs due to the complexity of their structures.[20] However, amorphous SSEs are also likely to exhibit high ionic conductivity;[21] for example, the Li_2S–P_2S_5 glass system has been extensively studied as SSEs.[22] Previously studied amorphous SSEs are mostly sulfides or oxides, but with the emergence of crystalline halide electrolytes,[23] some amorphous oxychloride electrolytes with good conductivity and compressibility began to appear. Hu *et al.*[24] synthesized partially amorphous oxychloride $Li_{1.75}ZrCl_{4.75}O_{0.5}$ which shows an ionic conductivity of 2.42 mS cm^{-1} at room temperature. Zhang *et al.*[25] presented amorphous SSEs, xLi_2O–MCl_y (M = Ta or Hf, $0.8 \leq x \leq 2$, $y = 5$ or 4) possessing ionic conductivities up to 6.6 mS cm^{-1} at 25 °C. In addition, Dai *et al.*[26] reported glasses $MAlO_xCl_{4-2x}$ (MAOC, M = Li, Na, $0.5 < x < 1$) by doping O atoms in $LiAlCl_4$, and the ionic conductivity at room temperature of $Li_{1.0}AlO_{0.75}Cl_{2.5}$ reached ~1 mS cm^{-1}. These inherently metastable amorphous materials are relaxed liquids *via* the evolution of medium-range order from the glass transition temperature, exhibiting unique characteristics, resulting in special physical and chemical properties. The first-principles calculations on $MAlO_xCl_{4-2x}$ indicated that Al atoms are connected into chains through O or Cl, forming an Al chain skeleton in these structures and the motion of Li and Cl has a correlation.[26] Although the preliminary understanding of amorphous SSEs has been obtained in our previous studies,[26,27] the formation mode of the disordered atomic arrangement, the mechanism and characteristics of Li^+ ion transport, and the effect of the O/Cl ratio on the atomic structure and ionic conductivity are still unclear. It is necessary to further analyze this system to figure out the above questions and try to select the design criterion for the amorphous SSEs.

[a]*Beijing National Laboratory for Condensed Matter Physics, Institute of Physics, Chinese Academy of Sciences, Beijing 100190, China*

[b]*Center of Materials Science and Optoelectronics Engineering, University of Chinese Academy of Sciences, Beijing 100049, China*

[c]*School of Physical Sciences, University of Chinese Academy of Sciences, Beijing 100049, China*

[d]*School of Materials Science and Engineering, Key Laboratory of Aerospace Materials and Performance (Ministry of Education), Beihang University, Beijing 100191, China. E-mail: rjxiao@iphy.ac.cn; hli@iphy.ac.cn*

† Electronic supplementary information (ESI) available. See DOI: https://doi.org/10.1039/d4ta06234e

To deepen the understanding of amorphous solid-state electrolytes, we generate and simulate the disordered Li–Al–O–Cl system in various compositions through *ab initio* molecular dynamics (AIMD), which is a relatively accurate method commonly used for crystalline systems in the simulation of structural evolution and ionic transport.[28,29] However, compared to crystals, computational simulation by AIMD has some unique challenges for amorphous materials. Firstly, the atomic arrangement of amorphous materials exhibits long-range disorder without translational periodicity symmetry, which makes it difficult to establish atomic models for simulation. Typically, the construction of the amorphous model in AIMD simulation is performed in a fictitious cubic box through melting and a rapid quenching process to obtain the disordered arrangement of atoms.[30] Due to the large computational cost of this method, the systems that are adopted in simulations are generally smaller than 200 atoms, corresponding to a lattice length of 10–20 Å. The size effect of the model and the accessible time scale for evolution become the main limitations for simulation effectiveness. Secondly, room-temperature ionic conductivity in amorphous configurations cannot be extrapolated from high-temperature results as crystals, as amorphous configurations constantly relax, leading to different structures at different temperatures. Direct simulations at room temperature are only possible for systems with high ion transport capabilities, as weak transport cannot generate enough migration events in a limited simulation time to obtain accurate statistical results. Thus although AIMD can accurately illustrate each conducting event and ion transport mechanism,[31–33] as well as provide us with initial configurations of disordered structures and simulate ion migration within a certain range, research on larger-spatial and longer-time scales and obtaining macroscopic overall ionic conductivity requires faster computational methods, such as recently developed machine learning interatomic potential based molecular dynamics (MLIP-based MD).

In this work, five different compositions for amorphous LAOCs ($Li_{0.5}AlO_{0.75}Cl_2$, $Li_{1.0}AlO_{0.75}Cl_{2.5}$, $Li_{1.5}AlO_{0.75}Cl_3$, $Li_{1.0}AlO_{0.25}Cl_{3.5}$ and $Li_{1.0}AlCl_4$) were simulated through the AIMD method and MLIP method to analyze the atomic structural and ion conducting characteristics on larger and longer scales, identify the physical origin of the excellent Li^+ transport performance of amorphous oxychloride, and present possible strategies to explore amorphous SSEs.

2 Results and discussion

2.1 Structural characteristics of LAOCs

The initial atomic structures for amorphous LAOCs are built through AIMD simulations through melting and a quenching process, for which the detailed method and parameters are described in the ESI.† The most significant feature of amorphous structures is the Al-chains formed by corner- or edge-sharing tetrahedra as shown in Fig. 1a. For comparison, crystalline $LiAlCl_4$ is illustrated in Fig. S1.† By comparing the cell volumes of crystalline and amorphous $LiAlCl_4$, it was found that the amorphous structure (2677 $Å^3$/96 atoms) has a larger cell volume than the crystalline structure (2552 $Å^3$/96 atoms), which is consistent with the characteristic that the volume of amorphous structures is slightly larger than that of their corresponding crystal structures supported by the free-volume model of the amorphous phase.[34] In addition, the change in Al-chain length during AIMD simulation of $Li_{1.0}AlO_{0.75}Cl_{2.5}$ is shown in Fig. S2.†

$Li_{1.0}AlO_{0.75}Cl_{2.5}$ is used to illustrate the structural characteristics of amorphous LAOCs. As shown in Fig. 1a, the structure contains long chains consisting of AlO_mCl_{4-m} (m = 1, 2, 3, 4) tetrahedra (AOC), and the Al atom on the chains is labeled as Al_{chain}. Isolated AOC tetrahedra also exist, and the Al atom in the center of isolated AOC tetrahedra is marked as Al_{iso}. In $Li_{1.0}AlO_{0.75}Cl_{2.5}$, two types of Al atom chains are found according to the number of Al atoms in the chain, which are Al5 and Al6 as illustrated in Fig. 1b and c. As we can see, Al atoms are connected by Cl or O atoms in the structure to form Al chains, and when the two adjacent Al_{chain} are connected by Cl atoms, the distance between them reaches a maximum not exceeding 4.2 Å. Therefore, in the analysis of other compositions, the Al atoms with distances less than 4.2 Å are considered to belong to the same chain. The statistical results on the percentage of Al chains with different chain lengths for each LAOC are presented in Fig. 1d. It shows that Al atoms in $Li_{0.5}AlO_{0.75}Cl_2$ are all Al_{chain}, forming Al16 chains. This chain contains 16 Al atoms, and the AOC tetrahedra are mostly connected in an Al–O–Al form, indicating that the formation of these long chains may be related to the high oxygen content in the structure. As the O/Cl ratio decreases, the number of Al_{chain} gradually decreases and the number of Al_{iso} increases, and when the doping concentration of O decreases to 0, the amorphous $Li_{1.0}AlCl_4$ contains the most Al_{iso}. It is noted that $Li_{1.5}AlO_{0.75}Cl_3$ and $Li_{1.0}AlO_{0.25}Cl_{3.5}$ have the same proportion of Al_{chain} and Al_{iso}, possibly originating from the limited simulation cells used in AIMD and the larger simulation box may exhibit more abundant structural details, thus better distinguishing these two structures. The structural characteristics also reflect in the radial distribution function (RDF) of the Al–Al pair in Fig. S3 and S4.† The first coordination in the Al–Al RDF curve of amorphous LAOCs originates from two adjacent Al_{chain}, since r (distance between Al–Al) is between 2 and 4 Å which is exactly the range for distances between adjacent Al_{chain}. As the O/Cl ratio decreases, the first coordination number gradually decreases, indicating that the number of Al_{iso} increases and the number of Al_{chain} decreases. The above findings indicate that the length and proportion of Al chains in the LAOC structure can be controlled by adjusting the O/Cl ratio. Finally, as Fig. 1e shows, Al_{chain} and Al_{iso} in $Li_{1.0}AlO_{0.75}Cl_{2.5}$ are distributed in a random way with no segregation phenomenon, which means the structure of LAOC is more similar to that of polymers formed by chains of various lengths.

2.2 Ionic transport mechanism of LAOCs

Since the local environment of Al in the LAOC structure are classified into Al_{chain} and Al_{iso}, the transport events of Li^+ ions can be divided into intra-chain transport, inter-chain transport,

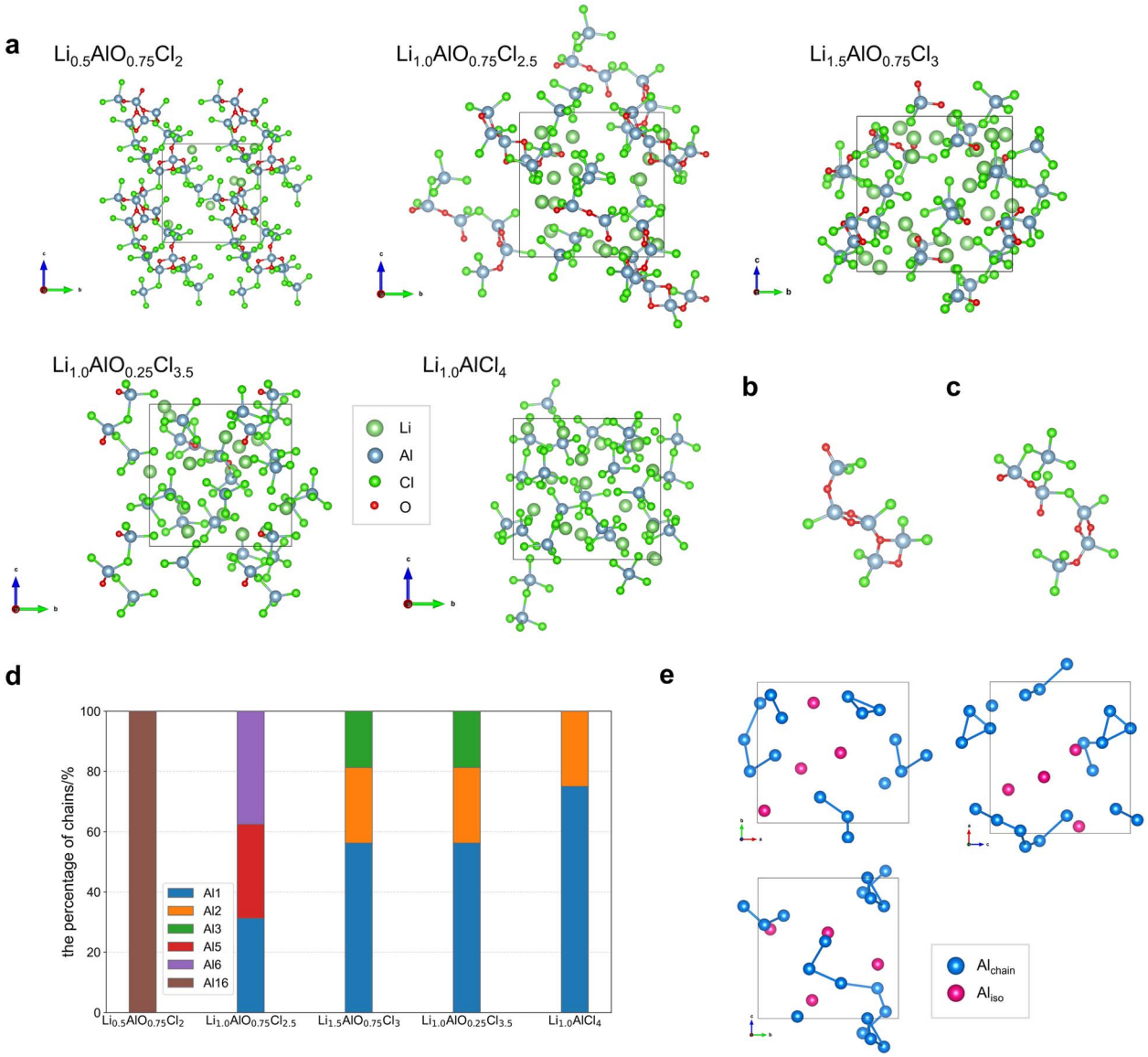

Fig. 1 Structural analysis of LAOCs calculated by AIMD. (a) The structures of amorphous LAOCs in five compositions. (b) Al5 and (c) Al6 chains found in the $Li_{1.0}AlO_{0.75}Cl_{2.5}$ structure. (d) The percentage of various Al chains in each of the five structures (for example, Al16 refers to an Al chain of 16 Al atoms). (e) The distribution of Al_{chain} and Al_{iso} in the $Li_{1.0}AlO_{0.75}Cl_{2.5}$ structure viewed in different directions.

and transport assisted by Al_{iso}. In these structures, Li^+ ions are connected to the Al-chains through either Cl^- or O^{2-}. Intra-chain transport refers to the migration of Li^+ from one AOC tetrahedron to another one in the same chain and inter-chain transport is the migration of Li^+ from a site bonding to one chain to the adjacent site connecting to another chain or another isolated AOC tetrahedron. Transport assisted by isolated Al refers to the migration of Li from one isolated AOC tetrahedron to another local environment (Fig. 2a).

We conduct a statistical analysis by calculating the proportions of Li^+ transport events and their nearest local environment of LAOCs in a 11–50 ps AIMD simulation. The specific statistical methods and processes of the migration of Li^+ ions in LAOC structures are demonstrated in Note S1.† The percentage of three different transport events of each LAOC composition at 300 K is displayed in Fig. 2b. The results revealed that as the O/Cl ratio decreases, the intra-chain transport gradually decreases, while the inter-chain and Al_{iso}-assisted transport increase. This is related to the change in atomic structure, in which the length and number of Al chains are gradually decreasing. The chemical environments for all the Li^+ migration events are analyzed and the conditions beneficial to Li^+ transport are extracted. Fig. 2c indicates the percentage of various tetrahedra in the initial structure (left column) and the percentage of tetrahedral types related to Li^+ transport events (right column). This suggests that the majority of the tetrahedra near the migrating Li^+ are $AlCl_4$ and $AlOCl_3$ tetrahedra (over 75%), indicating that the migration of Li^+ ions is more likely to occur in localized environments with high chlorine content. Furthermore, according to the analysis of the structural features

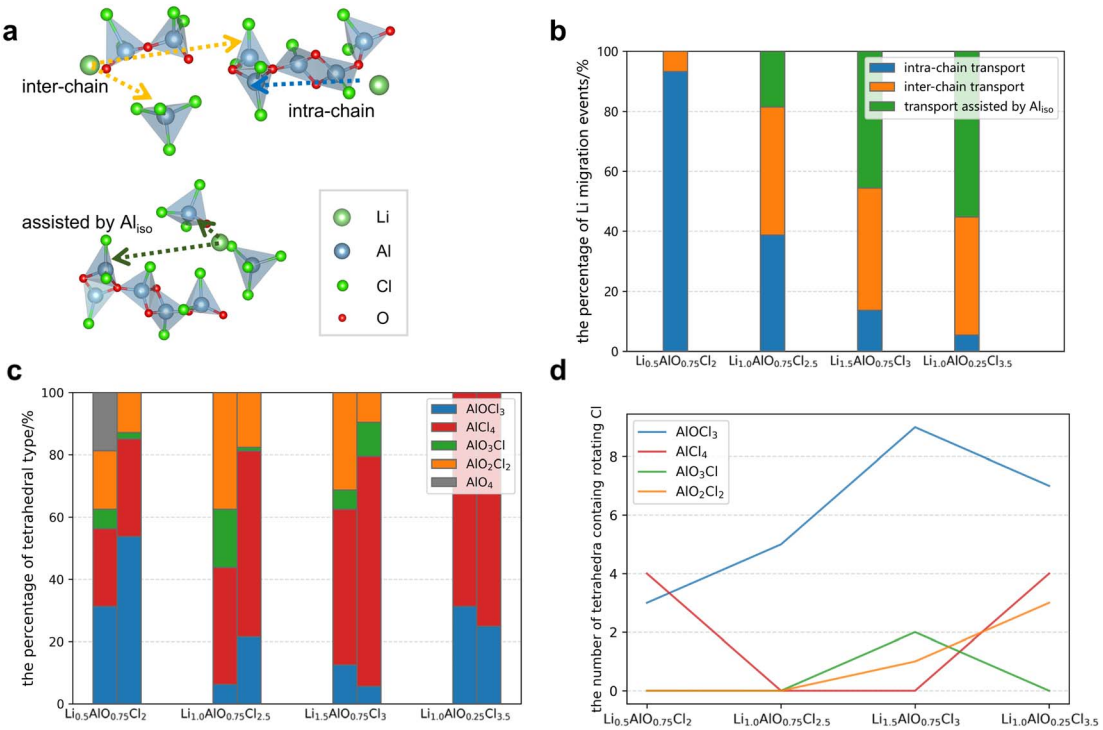

Fig. 2 Analysis of ion transport events in LAOCs calculated by AIMD. (a) Schematic diagram of the intra-chain transport event, inter-chain transport event and transport event assisted by Al_{iso}. (b) The percentage of three different transport events in LAOCs in 300 K's AIMD simulations within the range of 11–50 ps. (c) For each composition, left column: the percentage of the five tetrahedral types in the original structure of LAOCs; right column: the percentage of tetrahedral types located nearest to the migrating Li^+ ions in all transport events in LAOCs. (d) The number of tetrahedral types with rotating Cl atom in LAOCs.

mentioned earlier, O atoms mainly serve as corner- or edge-sharing atoms to connect tetrahedra, and hence a higher chlorine content implies a shorter Al chain length. Therefore, under the same conditions, the higher the sum of the tetrahedral ratios of $AlCl_4$ and $AlOCl_3$ in structures, the shorter the Al chains, and the higher the ionic conductivity expected to be found. While Li^+ migrates in the disordered structures, for Cl atoms, unlike remaining stably unmoved in crystal $LiAlCl_4$ (Fig. S5†), some Cl atoms also move in LAOCs, and as shown in Fig. 3c and S6,† the MSD of Cl is quite large. Different from Li, the Cl atom mostly rotates around the central Al of the AOC tetrahedron, without undergoing long distance migration. The changes in the Al–Cl bond lengths throughout the entire simulation process are shown in Fig. S7,† indicating that the Al–Cl bonds are not broken, demonstrating that Cl moves by rotation in its AOC tetrahedron. The only exception is the migration of one Cl atom connected with an $AlOCl_3$ tetrahedron in $Li_{1.0}AlO_{0.25}Cl_{3.5}$. Fig. 2d shows the tetrahedra with rotating Cl in different compositions proving that Cl movement on $AlCl_4$ and $AlOCl_3$ is the most intense, indicating that the rotation of Cl on $AlCl_4$ as well as $AlOCl_3$ and Li^+ transport can promote each other.

The above analysis indicates that the rotation of Cl within AOC tetrahedra of LAOC structures promotes the transport of Li^+ ions. Compared with AlO_2Cl_2, AlO_3Cl, and AlO_4, the proportion of stable O atoms on the tetrahedra of $AlCl_4$ and $AlOCl_3$ is smaller, and the inhibitory effect on the rotation of Cl connected to the same Al atom is also smaller. At the same time, the proportion of Cl atoms is higher, so once a Cl rotates, it is likely to drive the rotation of the surrounding Cl atoms. Therefore, the rotation of Cl on $AlCl_4$ and $AlOCl_3$ is much more intense than in others. When the ratio of $AlCl_4$ and $AlOCl_3$ is high, it can greatly promote the movement of Li^+. Therefore, in amorphous LAOCs, at the same Li and Al concentrations, the lower the O/Cl ratio (the more Cl atoms), the more intense the Li^+ transport, and the higher the expected Li^+ conductivity.

To prove the aforementioned conclusion, amorphous $Li_{1.0}AlCl_4$, $Li_{1.0}AlO_{0.25}Cl_{3.5}$ and $Li_{1.0}AlO_{0.75}Cl_{2.5}$, with the same concentration of Li and Al, were selected. According to the above analysis, the ion conductivity performance among these structures should be: $Li_{1.0}AlCl_4$ > $Li_{1.0}AlO_{0.25}Cl_{3.5}$ > $Li_{1.0}AlO_{0.75}Cl_{2.5}$. To confirm the inference, the AIMD simulations were conducted for these systems at 300 K, from which the statistically obtained MSDs are shown in Fig. 3b. Due to the size effect and a lack in statistical samples at large time intervals,[35] the Li^+ MSDs in Fig. 3b show plateaus, and here the values of MSDs are adopted to qualitatively compare the ion transport capability among different structures. The ionic conductivity will be estimated according to MLIP-based MD later. The MSD of the three structures is ranked as $Li_{1.0}AlCl_4$ > $Li_{1.0}AlO_{0.25}Cl_{3.5}$ > $Li_{1.0}AlO_{0.75}Cl_{2.5}$, which further confirms the correctness of the above conclusions.

Based on the above analysis, it is inferred that the doping effect of O in LAOC on Li^+ ion transport is a result of two factors.

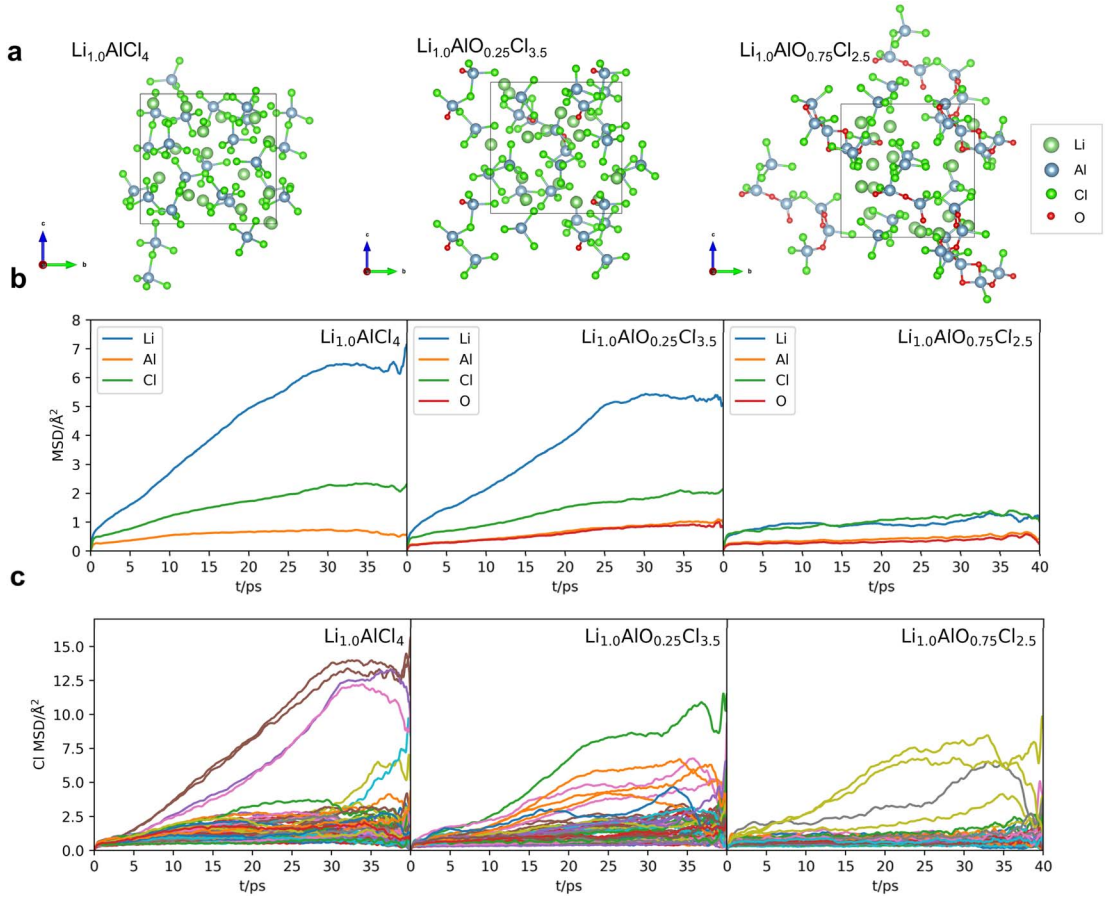

Fig. 3 Structures and MSDs of amorphous $Li_{1.0}AlCl_4$, $Li_{1.0}AlO_{0.25}Cl_{3.5}$ and $Li_{1.0}AlO_{0.75}Cl_{2.5}$ calculated by AIMD at 300 K. (a) The simulation models of $Li_{1.0}AlCl_4$, $Li_{1.0}AlO_{0.25}Cl_{3.5}$ and $Li_{1.0}AlO_{0.75}Cl_{2.5}$. (b) MSDs for $Li_{1.0}AlCl_4$, $Li_{1.0}AlO_{0.25}Cl_{3.5}$ and $Li_{1.0}AlO_{0.75}Cl_{2.5}$ at 300 K. (c) MSD of each Cl atom for $Li_{1.0}AlCl_4$, $Li_{1.0}AlO_{0.25}Cl_{3.5}$ and $Li_{1.0}AlO_{0.75}Cl_{2.5}$ at 300 K.

The addition of element O enhances the system's ability to form amorphous structures, promoting the rotation of Cl and the transport of Li. However, the decrease in Cl content reduces the number of $AlCl_4$ and $AlOCl_3$ tetrahedra, which has a negative effect on the transport performance of Li^+ ions. This also indicates that besides O doping, if we can find other ways to improve the amorphization degree of $LiAlCl_4$, it may be possible to achieve higher Li^+ ion conductivity at higher Cl content.

2.3 Machine learning interatomic potential based molecular dynamics (MLIP-based MD) simulation using large supercells

In AIMD simulations, the MSDs of lithium ions at 300 K in Fig. 3b are relatively small (<10 Å^2), indicating very few migration events which makes it difficult to evaluate the ion conductivity. Therefore, a larger cell and a longer period of simulation time are needed. Using the AIMD data as the training set, we obtained the MLIP for the Li–Al–O–Cl quaternary system through the DeePMD method,[32] which is one of the efficient softwares for training MLIP to accelerate the dynamic simulation process. The detailed training process is described in the ESI.† By adopting the MLIP-based MD, a large number of migration events occur during a longer simulation time and the ionic transport properties at 300 K are estimated. Note S2† provides the the accuracy validation of the MLIP model and the study of size effects used to determine the cell size for subsequent MLIP-based MD simulations.

To build the amorphous model in larger boxes such as 2 × 2 × 2 and 3 × 3 × 3 supercells expanded from the initial box for $Li_{1.0}AlO_{0.75}Cl_{2.5}$, two different modelling strategies are tested. Although both models have the same initial structure, which is the supercell expanded from the original disordered cell obtained from AIMD simulations, the first method involves a process of re-melting and quenching and then equilibrating by MLIP-based MD, while the second method directly conducts simulations at 300 K on the expanded structure using MLIP-based MD. Note S3† introduces a detailed description of these two methods. Fig. 4 illustrates the simulations' results for these two models in a 3 × 3 × 3 expanded box. Fig. 4a and b show that two methods yield very similar amorphous structures in $Li_{1.0}AlO_{0.75}Cl_{2.5}$, with a consistent distribution of the number of Al-chains and the proportion of AOC groups. However, model 1 has less Al_{iso} and fewer numbers of the sum of $AlCl_4$ and $AlOCl_3$ groups, resulting in a slightly lower ionic conductivity statistically evaluated from the MSD than that of model 2. An ionic conductivity of 12 mS cm^{-1} and 17 mS cm^{-1} was obtained for model 1 and model 2, respectively, indicating that due to the

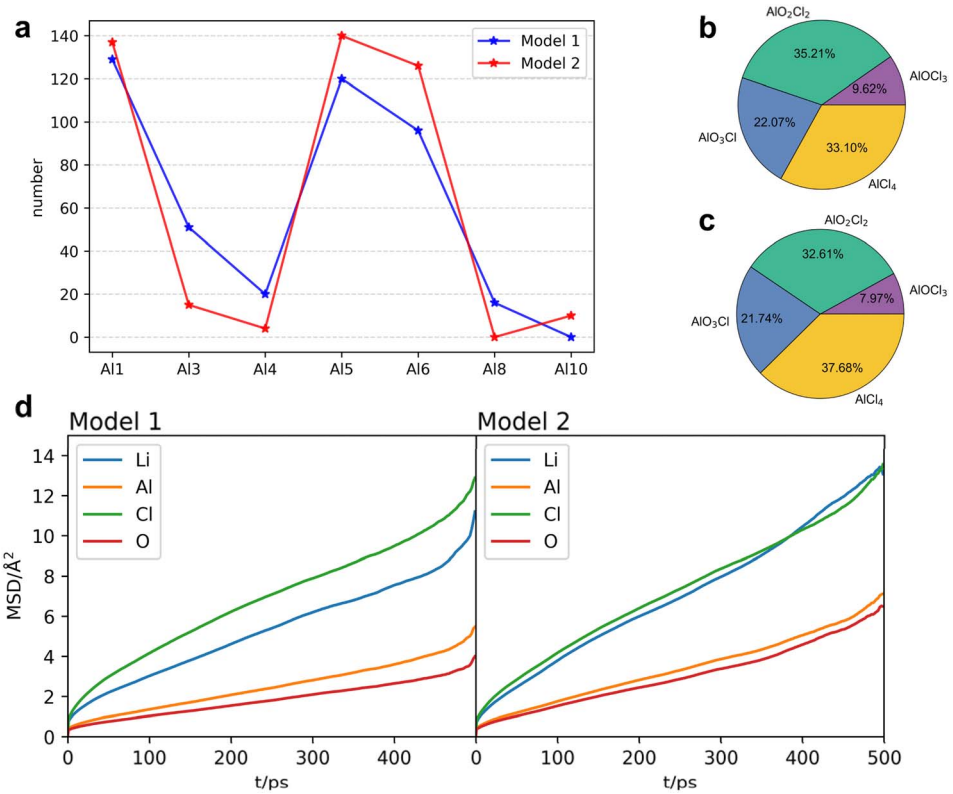

Fig. 4 Comparison of model 1 and model 2 for $Li_{1.0}AlO_{0.75}Cl_{2.5}$ calculated by MLIP-based MD simulations. (a) The number of Al chains of different lengths in two models of $Li_{1.0}AlO_{0.75}Cl_{2.5}$. (b) The percentage of the four tetrahedral types of $Li_{1.0}AlO_{0.75}Cl_{2.5}$ in model 1. (c) The percentage of the four tetrahedral types of $Li_{1.0}AlO_{0.75}Cl_{2.5}$ in model 2. (d) MSDs at 300 K for two models of $Li_{1.0}AlO_{0.75}Cl_{2.5}$.

non-uniqueness of the disordered structure, the ionic conductivity of the system varies with the degree of disorder. Since the disorder of the structure in the simulation is much higher than that of the experimentally synthesized structure, the calculated conductivity is also higher than that obtained experimentally (~1 mS cm^{-1} at 300 K (ref. 26)).

Therefore, we further investigated the relationship between Li^+ ion conductivity and the degree of disorder. Since only $LiAlCl_4$ has a definite crystal structure in the studied system, we used $LiAlCl_4$ structures at different melting stages to manufacture different degrees of disorder in the non-crystalline $LiAlCl_4$ configurations. The AIMD simulations at 300 K were carried out for these models with various amorphous degrees. The results in Fig. S8† indicate that in $LiAlCl_4$ more disordered structures show larger MSD values, which means higher Li^+ conductivity and more rotation events of Cl in AOC groups.

3 Conclusions

By constructing the amorphous structure of the $Li_xAlO_yCl_{3+x-2y}$ system and simulating the Li^+ ion conductivity properties, we have gained insights into the atomic structural features, ion transport mechanisms, as well as the modulation of ion conductivity by using the composition and structure in this type of disordered solid-state electrolyte. Based on this type of system, we have drawn the following conclusions. Firstly, in atomic structural analysis, through O doping, the $AlCl_4$ groups originally existing in $LiAlCl_4$ crystals in isolation transform into AOC groups, which are connected by O and Cl to form a skeleton of Al-chains with varying lengths. By adjusting the doping amount of O, the chain length distribution of Al-chains in the structure can be regulated. The main function of O doping is to enhance the system's glass forming ability, making it easier to synthesize amorphous structures in experiments. Secondly, in the analysis of ion transport performance, Li^+ ions migrate in the structure *via* both inter-chain and intra-chain modes, and the rotational freedom of Cl in the AOC groups enhances the migration ability of Li^+ ions. Due to the promoting effect of Cl rotation on Li^+ transport, the higher the Cl/O ratio in the completely amorphous LAOC structure, the stronger the promoting effect on Li^+ motion, and the better the ion transport performance of the structure. On the other hand, the doping of O helps to realize the amorphization of the LAOC structure, which is a prerequisite for Cl atoms to rotate and promote Li motion. Therefore, the doping of O in LAOC leads to the combined effect of these two factors, maximizing Li^+ ion conductivity at optimal doping concentrations. Besides, attempting other ways to increase the amorphization of chlorides without reducing Cl content is also an interesting endeavor in the future. Thirdly, unlike in crystalline systems, the non-uniqueness of the amorphous structure prevents the interpolation of ion conductivity at room temperature or lower from high-temperature MD data, and thus the practicality of MLIP-based MD simulations of amorphous solid-state

electrolytes was demonstrated and the ion conductivity was evaluated. Our simulations also indicate that even for structures with the same composition, the varying degrees of amorphization will result in different Li^+ ion conductivities. This provides an opportunity to adjust the amorphization degree of the system through control of synthesis conditions, thereby tuning the ionic conductivity performance.

Data availability

Original data are available upon request to be sent to the corresponding author of the paper.

Author contributions

R. J. X. managed and designed the project, checked the manuscript and provided suggestions. Q. F. Y. performed all theoretical calculations and provided related explanations, and drafted the manuscript, which underwent thorough revision with active participation and contributions from all authors. J. X., X. F., J. C. L., L. Q. W., and X. H. G. provided suggestions for the theoretical calculations and manuscript.

Conflicts of interest

The authors declare no competing financial interest.

Acknowledgements

This work was supported by funding from the National Natural Science Foundation of China (grant no. 52172258) and the Strategic Priority Research Program of Chinese Academy of Sciences (grant no. XDB0500200). The numerical calculations in this study were carried out on both the ORISE Supercomputer, and the National Supercomputer Center in Tianjin.

References

1 J. Janek and W. G. Zeier, *Nat. Energy*, 2023, **8**, 230–240.
2 J. C. Li, C. Ma, M. F. Chi, C. D. Liang and N. J. Dudney, *Adv. Energy Mater.*, 2015, **5**, 1401408.
3 S. Y. Wei, S. M. Xu, A. Agrawral, S. Choudhury, Y. Y. Lu, Z. Y. Tu, L. Ma and L. A. Archer, *Nat. Commun.*, 2016, **7**, 11722.
4 K. Takada, *Acta Mater.*, 2013, **61**, 759–770.
5 H. Akitoshi, S. Atsushi and T. Masahiro, *Front. Energy Res.*, 2016, **4**, 25.
6 F. Zheng, M. Kotobuki, S. F. Song, M. O. Lai and L. Lu, *J. Power Sources*, 2018, **389**, 198–213.
7 Y. Zheng, Y. Z. Yao, J. H. Ou, M. Li, D. Luo, H. Z. Dou, Z. Q. Li, K. Amine, A. P. Yu and Z. W. Chen, *Chem. Soc. Rev.*, 2020, **49**, 8790–8839.
8 G. Yang, Y. D. Song, Q. Wang, L. B. Zhang and L. J. Deng, *Mater. Des.*, 2020, **190**, 108563.
9 H. Yang and N. Q. Wu, *Energy Sci. Eng.*, 2022, **10**, 1643–1671.
10 J. Lau, R. H. DeBlock, D. M. Butts, D. S. Ashby, C. S. Choi and B. S. Dunn, *Adv. Energy Mater.*, 2018, **8**, 1800933.
11 J. Gao, Y. S. Zhao, S. Q. Shi and H. Li, *Chin. Phys. B*, 2016, **25**, 018211.
12 C. Yu, F. P. Zhao, J. Luo, L. Zhang and X. L. Sun, *Nano Energy*, 2021, **83**, 105858.
13 P. Adeli, J. D. Bazak, K. H. Park, I. Kochetkov, A. Huq, G. R. Goward and L. F. Nazar, *Angew. Chem., Int. Ed.*, 2019, **58**, 8681–8686.
14 L. D. Zhou, A. Assoud, Q. Zhang, X. H. Wu and L. F. Nazar, *J. Am. Chem. Soc.*, 2019, **141**(48), 19002–19013.
15 N. Kamaya, K. Homma, Y. Yamakawa, M. Hirayama, R. Kanno, M. Yonemura, T. Kamiyama, Y. Kato, S. Hama, K. Kawamoto and A. Mitsui, *Nat. Mater.*, 2011, **10**, 682–686.
16 Y. Kato, S. Hori, T. Saito, K. Suzuki, M. Hirayama, A. Mitsui, M. Yonemura, H. Iba and R. Kanno, *Nat. Energy*, 2016, **1**, 16030.
17 J. Y. Luo and Y. Y. Xia, *Adv. Funct. Mater.*, 2007, **17**, 3877–3884.
18 J. F. Wu, E. Y. Chen, Y. Yu, L. Liu, Y. Wu, W. K. Pang, V. K. Peterson and X. Guo, *ACS Appl. Mater. Interfaces*, 2017, **9**, 1542–1552.
19 C. Bernuy-Lopez, W. Manalastas, J. M. L. del Amo, A. Aguadero, F. Aguesse and J. A. Kilner, *Chem. Mater.*, 2014, **26**, 3610–3617.
20 Z. A. Grady, C. J. Wilkinson, C. A. Randall and J. C. Mauro, *Front. Energy Res.*, 2020, **8**, 218.
21 J. W. Ding, D. F. Ji, Y. Z. Yue and M. M. Smedskjaer, *Small*, 2024, **20**, 2304270.
22 M. Agostini, Y. Aihara, T. Yamada, B. Scrosati and J. Hassoun, *Solid State Ionics*, 2013, **244**, 48–51.
23 T. Asano, A. Sakai, S. Ouchi, M. Sakaida, A. Miyazaki and S. Hasegawa, *Adv. Mater.*, 2018, **30**, 1803075.
24 L. Hu, J. Z. Wang, K. Wang, Z. Q. Gu, Z. W. Xi, H. Li, F. Chen, Y. X. Wang, Z. Y. Li and C. Ma, *Nat. Commun.*, 2023, **14**, 3807.
25 S. M. Zhang, F. P. Zhao, J. T. Chen, J. M. Fu, J. Luo, S. H. Alahakoon, L. Y. Chang, R. F. Feng, M. Shakouri, J. W. Liang, Y. Zhao, X. N. Li, L. He, Y. N. Huang, T. K. Sham and X. L. Sun, *Nat. Commun.*, 2023, **14**, 3780.
26 T. Dai, S. Y. Wu, Y. X. Lu, Y. Yang, Y. Liu, C. Chang, X. H. Rong, R. J. Xiao, J. M. Zhao, Y. H. Liu, W. H. Wang, L. Q. Chen and Y. S. Hu, *Nat. Energy*, 2023, **8**, 1221–1228.
27 S. Y. Wu, R. J. Xiao, H. Li and L. Q. Chen, *Inorganics*, 2022, **10**, 45.
28 X. Fu, Y. Q. Wang, J. Xu, Q. F. Yang, H. C. Mao, R. J. Xiao and H. Li, *J. Mater. Chem. A*, 2024, **12**, 10562–10570.
29 J. Xu, Y. Q. Wang, S. Y. Wu, Q. F. Yang, X. Fu, R. J. Xiao and H. Li, *ACS Appl. Mater*, 2023, **15**, 21086–21096.
30 A. Karthikeyan and K. J. Rao, *J. Phys. Chem. B*, 1997, **101**, 3105–3114.
31 S. Q. Hao and C. Wolverton, *J. Phys. Chem. C*, 2013, **117**, 8009–8013.
32 J. L. Cheng, E. Sivonxay and K. A. Persson, *ACS Appl. Mater. Interfaces*, 2020, **12**, 35748–35756.
33 J. G. Smith and D. J. Siegel, *Nat. Commun.*, 2020, **11**, 1483.
34 D. Turnbull and M. H. Cohen, *J. Chem. Phys.*, 1961, **34**, 120–125.
35 X. F. He, Y. Z. Zhu, A. Epstein and Y. F. Mo, *npj Comput. Mater.*, 2018, **4**, 18.